Numerical Study of the Trajectory, Penetration, and Interaction of Single and Tandem Jets in a Crossflow Using LES

Longlong Huang[1]; Kun Zhao[2]; and Gareth J. Bennett[3]

Abstract: In this paper, a large eddy simulation (LES) method was used to conduct a study on single and tandem jets in a crossflow, focusing particularly on their trajectory, penetration, and interaction. The numerical model was validated with an experimental test campaign. Examination of the time-averaged flow field allowed both the velocity and the tangential angle of the jet trajectories to be examined. In addition, the penetration depth of the jet based on a scalar transport model was analyzed. The unsteady flow characteristics around the trajectories were studied using both the power spectral density (PSD) function and a spectral proper orthogonal decomposition (SPOD). The results show that the upstream jet's trajectory changes little as a function of spacing, while the downstream jet deflects as a result of the influence of the counterrotating vortex pair. In addition, the curve height of the tandem jet trajectories is significantly higher than that of the single jet. The height of the trajectory formed by the tandem jets can reach four times that of the single jet, and the penetration depth of the tandem jets can be 2.8 times that of the single jet. Meanwhile, when the spacing between the two jets is small, the coherent structures tend toward the upstream jet distribution, and the fluctuation frequency after mixing is dominated by the upstream jet. With the increase of spacing, the fluctuation frequency after mixing is greatly affected by the downstream jet, and the frequency decreases. Furthermore, when the dimensionless spacing D' is 5.67, the frequency difference between both jets is minimal and the coherent structures are significantly reduced, indicating that flow mixing is optimal and stable. **DOI: [10.1061/JAEEEZ.ASENG-5154](https://doi.org/10.1061/JAEEEZ.ASENG-5154)**. *© 2023 American Society of Civil Engineers.*

Author keywords: Jets in crossflow; Air curtain; Power spectral density (PSD); Spectral proper orthogonal decomposition (SPOD); Large eddy simulation.

Introduction

Single/tandem jets in crossflow (S/TJICFs), also referred to as the air curtain, are an interesting flow regime that consist of many complex flow phenomena, e.g., various vortices, jet interaction, flow instability, recirculation, and complex spanwise variations. S/TJICFs are often encountered in practical applications such as flow-induced noise reduction (Zhao et al. 2020a, b), tunnel smoke confinement, biological safety cabinet confinement, and blade cooling (Acharya et al. 2006; Zhao et al. 2018a, b; Luo et al. 2013; Huang and Chou 2009), and as such have attracted much research interest. Many researchers have performed studies on S/TJICF from different perspectives, e.g., vortical structure development (Fearn and Weston 1974; Santiago and Dutton 1997; Kiel et al. 2003), the effect of the jet number (Gutmark et al. 2011; Makihata and Miyai 1979), jet interaction (Isaac 1982; Isaac and Jakubowski 1985; Yu et al. 2006; Lai and Lee 2010), and effects of nozzle shape (Gutmark et al. 2008; Kumar et al. 2011). In the study of the jet in crossflow, the trajectory of S/TJICF has always been an important research focus because it helps to predict the overall flow field development. After the jet is ejected and penetrates the oncoming flow, the surrounding transverse momentum will be entrained, and the jet will change direction resulting in an oblique trajectory. To date, a small number of semiempirical equations have been proposed to describe the trajectory of an SJICF (Haniu and Ramaprian 1989; Yuan and Street 1998; No 2015; Shaw et al. 2020), which have been used, for example, in aeronautical engineering applications (Oerlemans and Bruin 2009; Zhao et al. 2018a). Regarding the TJICF, a few studies have been also conducted to qualitatively investigate the effect of additional jets on the primary jet's trajectory (Makihata and Miyai 1979; New and Zang 2015; Radhouane et al. 2019; Olyaei and Kebriaee 2020). However, no quantitative model has been made to predict the trajectory of a TJICF. As such, in this paper a model for the TJICF will be developed.

Another interesting research topic of S/TJICF is the penetration of the jet(s). In this paper, jet penetration variation against trajectory is studied. There are a few studies reported that concentrate on penetration, mostly on liquid jets in high-speed gas flows (Ghenai et al. 2009; Lin et al. 2002; Sathiyamoorthy et al. 2020). This configuration is of interest because it corresponds to liquid fuel being ejected into the gas flow inside an engine duct. However, when it comes to single-phase flow, where both the jets and the crossflow gases are the same, typically air, the problem is more challenging. More specifically, the jets and the crossflow will merge and it is difficult to distinguish their boundaries and assess the penetration. Simulation can be a very useful tool to conduct the analysis,

[1]Research Assistant, Key Laboratory of Aerodynamic Noise Control, Low Speed Aerodynamics Institute, China Aerodynamics Research and Development Center (CARDC), Mianyang, Sichuan 621000, China. Email: hlong9925@163.com

[2]Associated Professor, Key Laboratory of Aerodynamic Noise Control, Low Speed Aerodynamics Institute, China Aerodynamics Research and Development Center (CARDC), Mianyang, Sichuan 621000, China (corresponding author). ORCID: https://orcid.org/0000-0003-3077-3584. Email: zhaokun@cardc.cn

[3]Associated Professor, School of Engineering, Trinity College Dublin, Univ. of Dublin, Dublin D02 PN40, Ireland. ORCID: https://orcid.org/0000-0002-1621-7533. Email: gareth.bennett@tcd.ie

especially using a scalar transport (ST) model, which has been validated in the study of jet mixing (Ivanova et al. 2010; Ryan et al. 2017). Therefore, a numerical simulation approach was taken in this paper to study the jet penetration. Additionally, jet interaction, which affects other flow characteristics, is also discussed from the perspective of its relation to the trajectory. Unlike previous studies, this paper employed spectral and modal analysis, which results in some novel findings.

In this paper, S/TJICFs have been numerically simulated using large eddy simulations (LESs), validated by particle image velocimetry (PIV) in the FLy-17 0.55 m × 0.4 m aeroacoustic wind tunnel (China Aerodynamic Research and Development Center, Mianyang, China). Initially, in terms of time-averaged flow field, the trajectory of the TJICF was modeled and the vortex distribution, velocity, and tangential angle associated with the trajectory of S/TJICF were discussed. Then the penetration variation against trajectory was discussed, based on an approach to defining the level of penetration. Finally, interaction of the jets associated with the trajectory were discussed using power spectral density (PSD) and spectral proper orthogonal decomposition (SPOD) to investigate spectral analysis and modal analysis.

PIV Experiment

FL-17y Aeroacoustic Wind Tunnel

The experiment was conducted in the FLy-17 0.55 m × 0.4 m aeroacoustic wind tunnel at the China Aerodynamics Research and Development Center (CARDC), as shown in Fig. 1(a). FLy-17 is powered by a 130-kW axial fan, allowing the incoming flow U_∞ to be controlled within the range of 8–100 m/s. The nozzle outlet size is 0.55×0.4 m (height × width) and the test section is surrounded with a full anechoic room of $5.2 \times 3.7 \times 4$ m, illustrated in Fig. 1(b). Turbulence intensity in the core flow region is controlled to be ≤0.05%. The background noise is ≤75–80 dB ($U_\infty = 80$ m/s).

The S/TJICF rig plays a critical role in creating the necessary flow regime, whose detail is provided in Fig. 2. In the rig, the steady rectangular jet flow is generated by two separate 30-kW blowers. To manipulate the jet velocity, each blower was equipped with a frequency-control converter. The flow coming out of the blower goes through a hose and then enters a nozzle, which was designed with a diffusion section. In the diffusion section, one layer of honeycomb with a hexagonal grid was installed to reduce the turbulence level of the flow.

The test was carried out in the open-jet test section of a 0.5×0.4 m acoustic wind tunnel, whose maximum velocity in the open-jet section was 100 m/s as measured by hotwire anemometry. The axial gradient of static pressure was less than 0.005 Pa and the turbulence intensity was less than 0.05%. The crossflow, created by the wind tunnel, flows along the flat plate and interacts with the planer jet that is set at a distance T_1 from the nozzle of the wind tunnel. The nozzle of the jet with a width of w was connected to the guide air duct that provides a continuous air flow through the 30-kW centrifugal blower. The guide air duct mainly plays the role
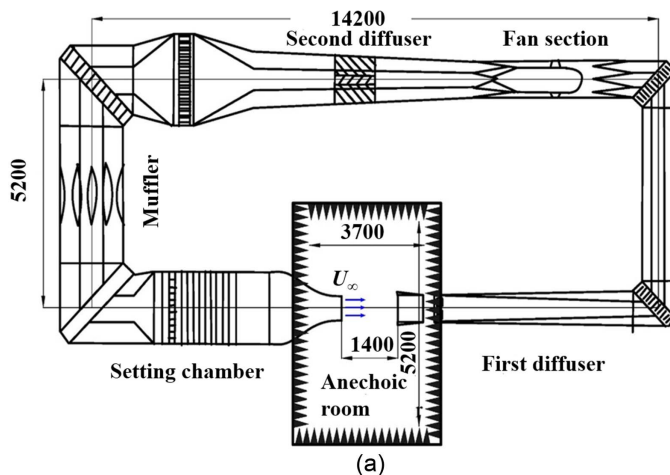

Fig. 1. FLy-17 0.55 m × 0.4 m aeroacoustic wind tunnel: (a) dimensions (mm); and (b) full view.
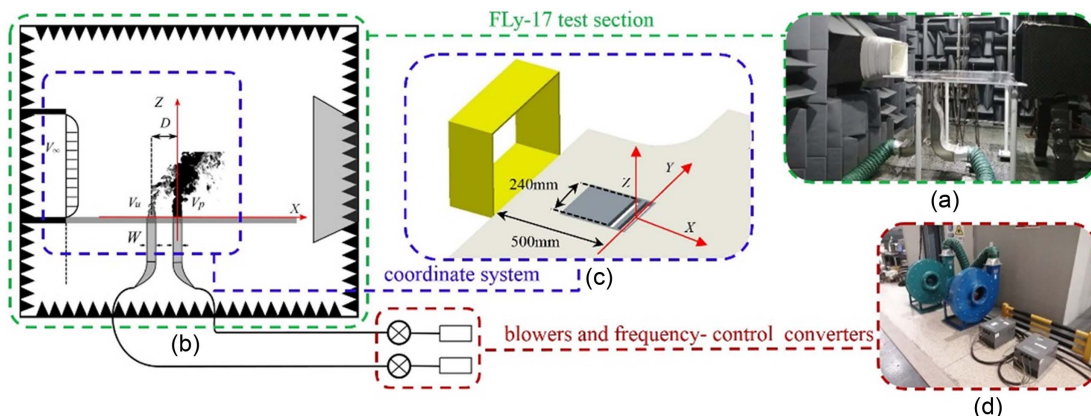

Fig. 2. Test platform: (a) wind tunnel; (b) nozzle of jet; (c) flat plate; and (d) guide air duct.
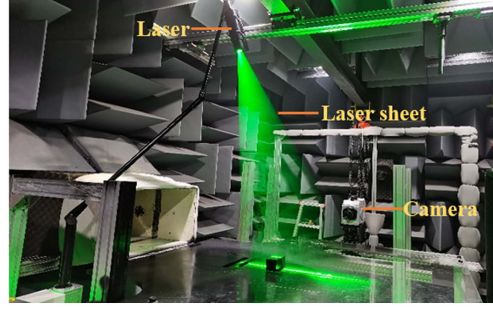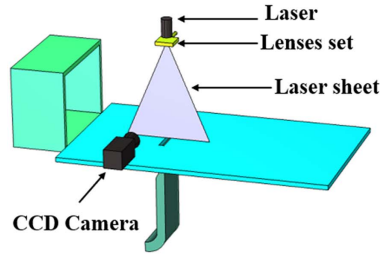
Fig. 3. PIV test.

of guiding the air flow, and it contains an aluminum rectifying honeycomb mesh, which can rectify the air flow well and improve its quality.

PIV Arrangement

A two-dimensional low-speed PIV system was used to carry out all flow measurements, which allow a quantitative analysis of the flow regime. To visualize the flow field, both the jets and the crossflow were seeded with Pea Soup Oil Based Smoke Generator PS31 (Pea Soup, Middlesbrough, UK). The size of the particles was on the order of 1.5 μm. The measurement plane was made to align with the center plane of the test section. The particles in the plane were illuminated using a sharp laser sheet. The source of the sheet was a New Wave Solo-II PIV double-pulsed Nd: YAG laser (532 nm, 30 mJ/pulse) mounted on the top of the aluminum frame. One lens set was used to diverge the point source to a line source. In addition, to highlight the illuminated plane, one black PVC board was fixed behind the laser sheet as a dark background. The board was outside the crossflow and accordingly had no interference with the flow.

A LaVision (Ypsilanti, Michigan) FlowMaster CCD camera was situated beside the test section, taking image pairs of the flow field of interest. A 532-nm narrowband pass optical filter was installed on the camera lens for the measurements. A three-dimensional computer-aided design (CAD) sketch of the PIV arrangement is shown in Fig. 3. The image pairs were captured at 4 frames per second, and the time delay between two images in one pair was 15 μs. The resolution of the CCD camera is 1,280 by 1,024 pixels. In the setup described, the image size was 106×84.6 mm ($X \times Y$). This allows the image to have a resolution of 12×12 pixels per square millimeter. Those image pairs were processed using cross-correlation in DaVis software with decreasing multipass interrogation window sizes, 32×32 and 16×16, respectively. There were two passes and a 50% overlap for each window size. The postprocessing was performed with an open access MATLAB toolbox, PIVMat.

Numerical Approach

LES Governing Equation

The LES equation of isothermal incompressible flow is

$$\frac{\partial \bar{u}_i}{\partial x_i} = 0$$
$$\frac{\partial \bar{u}_i}{\partial t} + \frac{\partial \bar{u}_i \bar{u}_j}{\partial x_j} = -\frac{1}{\rho}\frac{\partial \bar{p}}{\partial x_i} + \frac{\partial}{\partial x_j}(v2\bar{S}_{ij} - \tau_{ij}) \quad (1)$$

where $\bar{u}_i$ = velocity component; $\bar{p}$ = pressure of the fluid; ρ = density of the fluid; and ν = viscosity.

The strain tensor $\bar{S}_{ij}$ is expressed as follows:

$$\bar{S}_{ij} = \frac{1}{2}\left(\frac{\partial \bar{u}_i}{\partial x_j} + \frac{\partial \bar{u}_j}{\partial x_i}\right) \quad (2)$$

The compressive lattice stress is expressed as

$$\tau_{ij} = \overline{u_i u_j} - \bar{u}_i \bar{u}_j \quad (3)$$

The approximate Boussinesq formula is

$$\tau_{ij} - \frac{\delta_{ij}}{3}\tau_{kk} = -2v_{sgs}\bar{S}_{ij} \quad (4)$$

where ν_{sgs} = eddy viscosity model, and the formula is

$$v_{sgs} = (C_s\Delta)^2|\bar{S}| \quad (5)$$

Computational Domain and Boundary Conditions

Fig. 4 is a schematic diagram of the flow of the TJICF, and Fig. 5 is a numerical model of a TJICF. The size of the incoming flow inlet
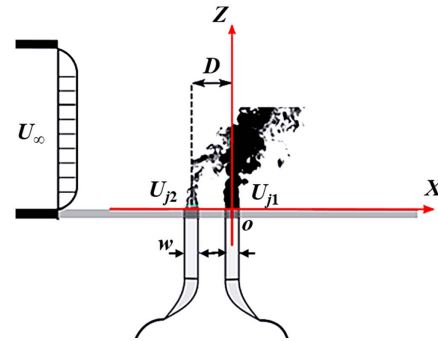

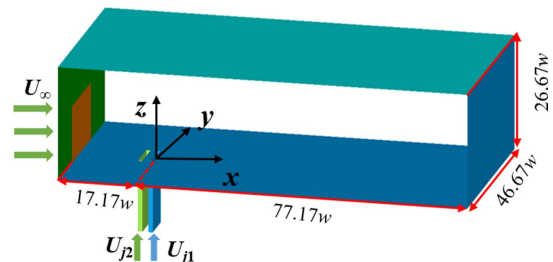**Fig. 4.** Schematic diagram of the flow.

Fig. 5. Numerical model.

Table 1. Simulation matrix

Case	U_∞ (m/s)	U_{j2} (m/s)	U_{j1} (m/s)	$q = U_{j2}/U_\infty$	D'	Configuration
1	50	—	40/50	—	—	Single jet
2	50	50	30	1	7.33	Tandem jets with different D,
3	50	50	30	1	5.67	Re = 108,101/64,860 ($U_{j2} > U_{j1}$)
4	50	50	30	1	4.00	
5	50	50	30	1	2.33	
6	50	30	50	0.6	2.33	$U_{j2} < U_{j1}$

is 0.55×0.4 m, the velocity U_∞ is 50 m/s, and the rectangular jet of size $w \times d$ is set at $17.17w$ away from the hole, where the nozzle width w is 30 mm. The distance between the centers of the two jets is D, and the dimensionless expression is $D' = D/w$. The velocity variation range of the tandem jets U_{j1} and U_{j2} is 30–50 m/s, and the momentum ratio $q = U_{j2}/U_\infty$. Symmetrical boundaries are used on the left and right sides. The time step is 2.5×10^{-5} s, and the total computation time is 0.5 s. The output contains the flow field data for the last 0.15 s, with a time step of 1.25×10^{-4} s. These data were used for time-averaged flow field analysis and spectral analysis. Table 1 gives the simulation matrix of different cases performed using a commercial solver COMSOL.

Meshing

Three kinds of structured grids with element numbers of 7.29 million, 9.9 million, and 12.03 million were used to verify the grid independence. The number of elements finally selected for the single jet was 12.03 million, and the total number of grids for the tandem jets was 14.48 million. Fig. 6 shows the grid distribution of different sections.

Simulation Verification

Fig. 7(a) shows the verification of grid independence for the single jet and the comparison between the test and simulation results, where the incoming flow was $U_\infty = 50$ m/s and the jet velocity was $U_{j1} = 40$ m/s. A line segment at the position of $X/w = -5$ and 5 on the central section of $Y = 0$ was selected to compare the velocity distribution. At the same time, a comparison was made between the streamline in Case 6 [Fig. 7(b)] and the trajectory of the upstream jet [Fig. 7(c)].

It can be seen from Fig. 7 that the velocity distributions with different element numbers are basically the same, and the
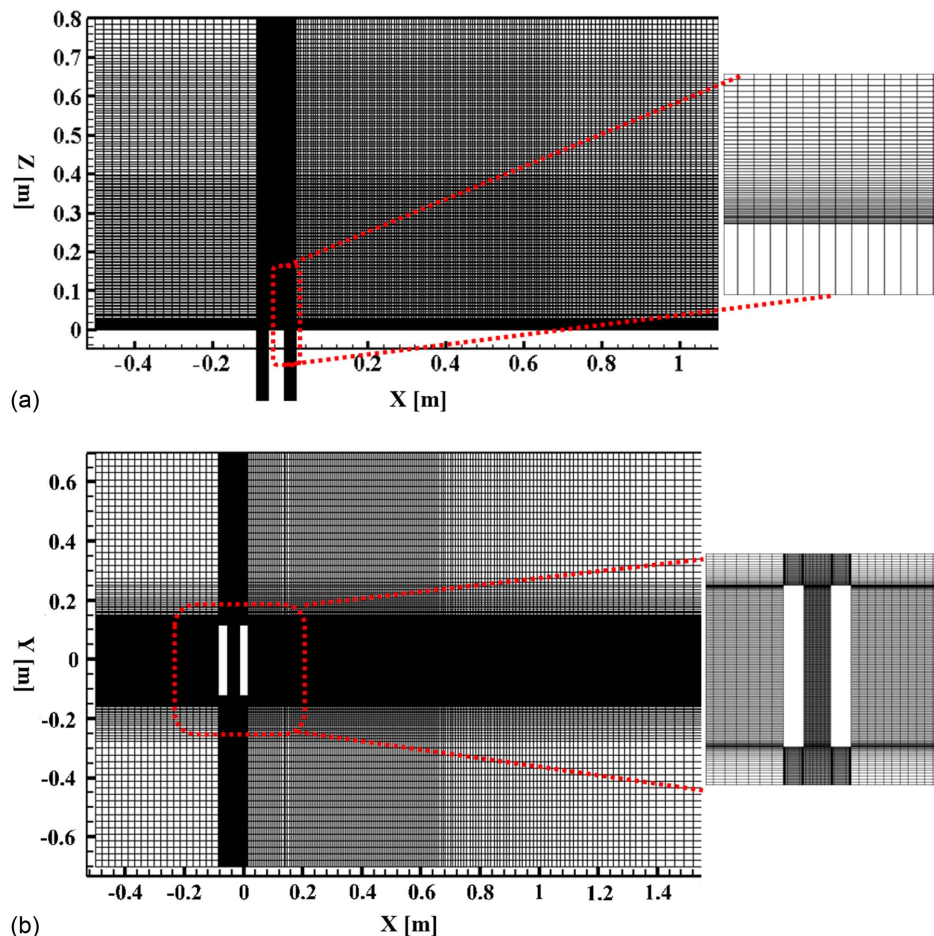

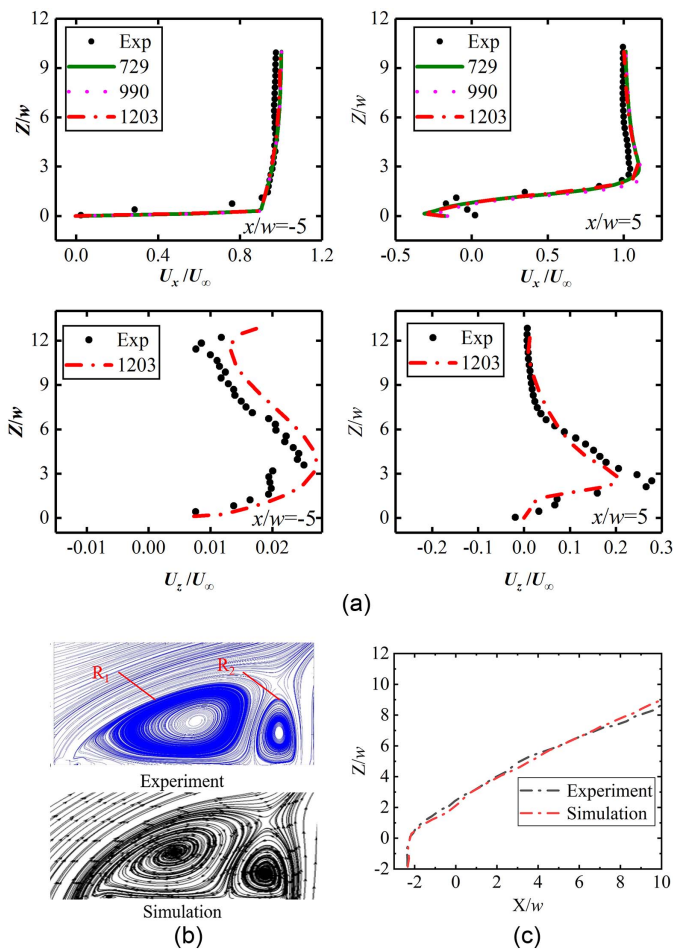**Fig. 6.** Meshing: (a) X-Z section; and (b) X-Y section.

Fig. 7. Simulation verification.

difference between the results is within 1%. Because LES requires a high number of elements, the grid selection for a single jet is 12.03 million. Second, the simulated velocity distributions on the left and right sides ($X/w = -5$ and 5) are in good agreement with the experimental results. Because the experimental measurement is not accurate enough for the boundary layer processing, and because the particle density near the boundary layer in the test is not high enough, there is a deviation between the test and simulation results in this area. In addition, it was found through the streamline distribution in Figs. 7(b and c) that the distribution of
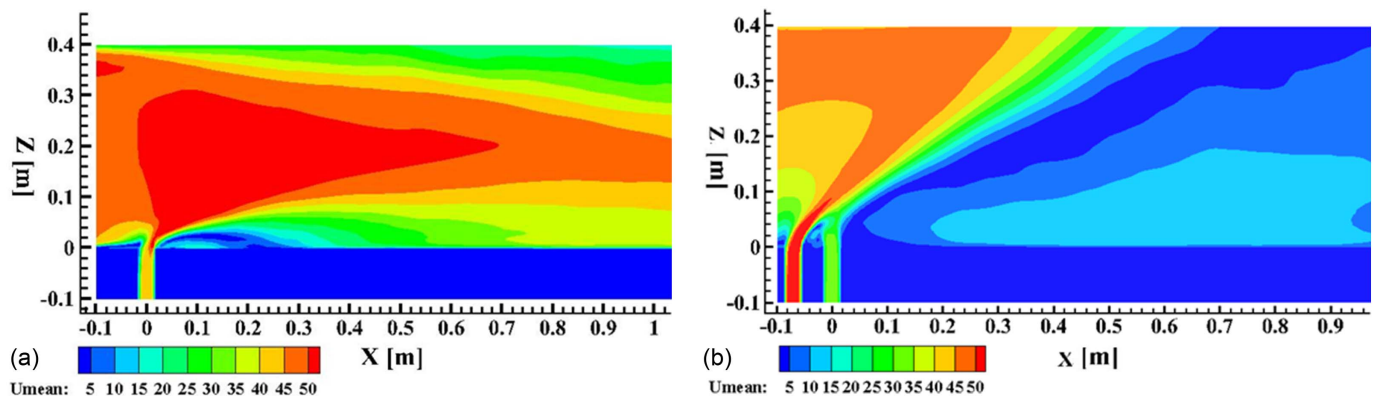
two counterrotating vortex pairs obtained from experiment and simulation, R_1 and R_2, have basically the same shape and size, and the trajectory curves of the upstream jets are consistent. In general, the simulation model is feasible.

Results and Discussion

This section provides the results from LES simulations, and a discussion from different aspects including trajectories of S/TJICF, penetration variation against trajectory, and spectral analysis and modal analysis.

Trajectories of S/TJICF

The trajectory of S/TJICF has always been an important research focus because it helps predict the overall flow field development.

Variation of Trajectories
Fig. 8 compares the trajectories of single and tandem jet time-averaged velocity magnitude contours respectively from Case 1 and Case 5. It can be clearly seen that the height of the downstream jet of TJICF is higher than that of the single jet of SJICF. Regarding this variation, the trajectory is a very good tool to perform an evaluation of performance.

There are a few options for defining the jet trajectory. Many researchers (Makihata and Miyai 1979; No 2015; Schetz et al. 1983; Yuan and Street 1998) use the maximum velocity or concentration in the central plane as the jet trajectory curve, but there are multiple maximum values near the jet outlet, making such a definition of the trajectory curve difficult. Therefore, the streamline that stems from the nozzle center has been mostly used as the jet trajectory (Pokharel and Acharya 2021), which is also adopted in this paper as well.

Figs. 9 and 10 show the trajectory curves of S/TJICF for different cases, which illustrate the comparison of the trajectory between two configurations. First, it can be seen from Fig. 9 that for the single jet, with the increase of jet velocity, the height of the trajectory rises as expected. Then, in Fig. 10, it can be detected that the trajectories in tandem jets, regardless of the upstream jet or the downstream jet, can go much higher and the maximum of the height can reach approximately four times that of the single jet. Moreover, in Fig. 10 it can be also found that under different spacing D, the upstream jet trajectory approximately remains with little change, while the downstream jet trajectory apparently increases with D'.
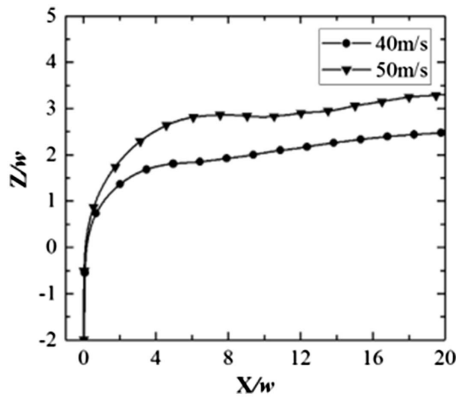

Fig. 8. Contours of time-averaged velocity magnitude: (a) single jet; and (b) tandem jets.
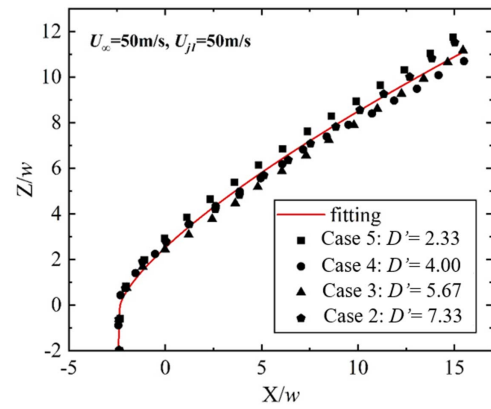
Fig. 9. Trajectory of single jet.

Fig. 11. Fitting curve of upstream jet trajectory.

Modeling of Trajectories

Modeling of the jet trajectories was conducted in this paper to give a further quantitative analysis of the trajectory variation. To date, most of the corresponding research on the trajectory has focused on circular jets, and various semiempirical equations have been obtained through dimensional analysis (No 2015; Yuan and Street 1998). In contrast, the rectangular jet penetrates deeper than the circular jet, delaying the vortex breakdown (Pokharel and Acharya 2021). According to the semiempirical formula of the circular jet trajectory equation, the rectangular jet trajectory equation is derived here by taking the momentum ratio q, jet diameter w, and trajectory coordinates X_i as parameters, expressed as

$$\frac{Z_i}{w} = A q^B \left(\frac{X_i - D}{w} \right)^C \tag{6}$$

where Z_i = height of the trajectory curve; w = width of the nozzle; $q = \rho_j U_{j2}^2 / \rho_\infty U_\infty^2$ is the momentum ratio of the upstream jet to the incoming stream; and A, B, and C = correlation coefficients of the formula.

It can be seen from Fig. 10(a) that the trajectory of different cases changes very little, and a semiempirical trajectory curve equation can be obtained through data fitting. However, the momentum ratio q in Eq. (6) is a fixed value, and $q = 0.6$ for Case 6 is different from $q = 1$ for Cases 2–5. For this reason, we use the data from Cases 2–5 to fit Eq. (6), and the fitting results are shown in Fig. 11 and Eq. (7):

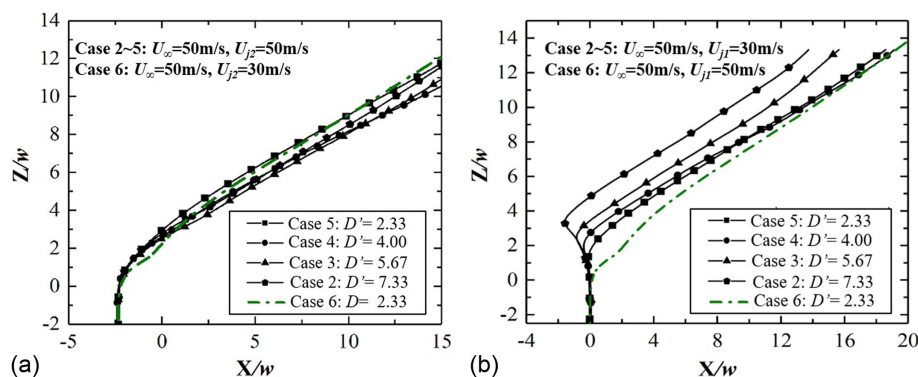$$\frac{Z_i}{w} = 1.36 q \left(\frac{X_i - D}{w} \right)^{0.73} \tag{7}$$

Table 2. Semiempirical formula correlation coefficient for the upstream jet trajectory curves

Case	Configuration	D'	A	B	C
5	Tandem jets with	2.33	1.4866	1	0.7242
4	different spacing D,	4.00	1.3027	1	0.7369
3	$q = 1$ ($U_{j2} > U_{j1}$)	5.67	1.0243	1	0.8319
2		7.33	1.5725	1	0.8041
6	$q = 0.6$ ($U_{j2} < U_{j1}$)	2.33	1.4009	0.4154	0.9219

We know that the momentum ratio q of Case 6 is different from that of Cases 2–5. When the momentum ratio q of Case 6 changes, the corresponding correlation coefficient B will also change, but the impact on A and C is unclear. At the same time, when D changes, the value of the correlation coefficient C will also be different, and whether it will affect A and B needs to be further studied. Therefore, to further study the effect of the momentum ratio q, as well as D, on the correlation coefficients A, B, and C, instead of the previous uniform fitting, we now make a separate fitting, and the values of the correlation coefficient are obtained by fitting the upstream trajectory curves for Cases 2–6, as shown in Table 2.

Through the analysis of Table 2, first, it is found that the change of B is mainly affected by the momentum ratio q, and is independent of D. The values of A and C are affected by both D and the momentum ratio q. Then, when D' is less than 5.67, A decreases and C increases. Instead, when D' is greater than 5.67, the change trend of A and C values is reversed. Therefore, $D' = 5.67$ is an important law for D for the TJICF.

Fig. 10. Trajectory of tandem jets: (a) upstream jet; and (b) downstream jet.
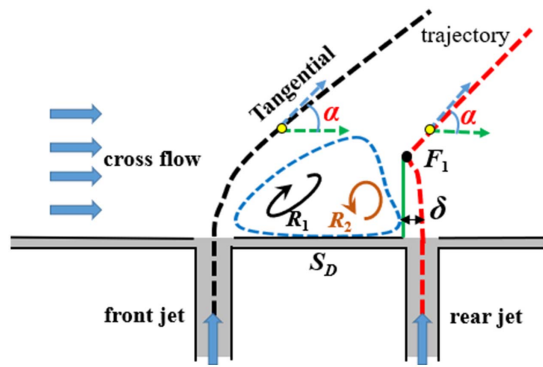
Fig. 12. Schematic diagram of TJICF.

Tangential Angle on the Trajectories

As clearly depicted, with flow conditions varying, the performance of the trajectory curves can differ significantly. To further study this, the change of trajectories, especially on the tangential angle, is discussed. TJICF is a complex flow, including many interesting flow characteristics, for example, those shown in Fig. 12. First, the trajectory formed by the upstream and downstream jets penetrating the incoming flow is shown in the figure, and the change characteristics of the trajectory can be determined by the tangential angle, α, of the trajectory, which is the angle between the tangential direction and the horizontal direction at any point. Then there is an interaction zone S_D between the two jets, in which two counterrotating vortex pairs R_1 and R_2 exist. During the flow process of the downstream jet, the trajectory of the downstream jet deflects to the left and reaches the maximum offset δ at the inflection point F_1 as a result of the adsorption of R_2. The tangential angle, α, of the trajectory at the inflection point F_1 is 90°, and the trajectory starts to deflect to the right after reaching the maximum offset.

Figs. 13 and 14 show the trajectory curves of the tandem jets and the streamline distributions, respectively. First, it can be seen from

Fig. 13 that the trajectory curves of the low-velocity jet will shift to the side of the high-velocity jet, and the maximum offset δ will be reached at the inflection point F_1. Second, according to the flow in S_D, when the D' is different, the size of the counterrotating vortex pair formed in the S_D area is also different. With increasing D', the sizes of R_1 and R_2 both decrease, and the vortex formed on the side with low jet velocity is larger. Moreover, with the increase of D', the fluid of the downstream jet adsorbed into the S_D area also increases, but only a small part of the fluid sucked into the S_D area forms vortex R_2.

The downstream jet deflects to the left in the flow process, mainly because the downstream jet has a lower velocity and forms a larger vortex R_2, which causes the downstream jet to deflect to the left under the effect of R_2 adsorption and reach the maximum offset δ at the inflection point F_1. To further quantitatively analyze the change characteristics of tangent angle of trajectory curve under different cases, the tangent angle α and maximum offset δ of trajectory with different spacing D' were obtained as shown in Fig. 15, where Figs. 15(a and b) correspond to upstream jet and downstream jet, respectively. In Fig. 15(b), on the one hand, the trajectory on the left side of F_1 deflects to the left, so $\alpha < 0$; on the other, the trajectory on the right side of F_1 deflects to the right, so $\alpha > 0$. The maximum offset of δ was reached at point F_1. Tangential angle change $\Delta\alpha_{\max}$ on the left side of F_1 reaches the maximum at the peak value in Fig. 15(b). The maximum tangential angle change $\Delta\alpha_{\max}$ and δ are shown in Table 3 and Fig. 16.

To begin with, it can be seen from Fig. 15(a) that because the upstream jet is between the incoming jet and the downstream jet, its flow fluctuation is limited, so at different spacing D', the change of the tangential angle α of the upstream jet is small. In Areas I and II, the change of tangential angle α with spacing $D' = 2.33$ and 7.33 is closer. Additionally, from Fig. 15(b) and Table 3, it can be detected that the maximum change of tangential angle $\Delta\alpha_{\max}$ of the downstream jet trajectory and offset δ both increase with D'. More specifically, it is found from Fig. 16 that with the increase of D',
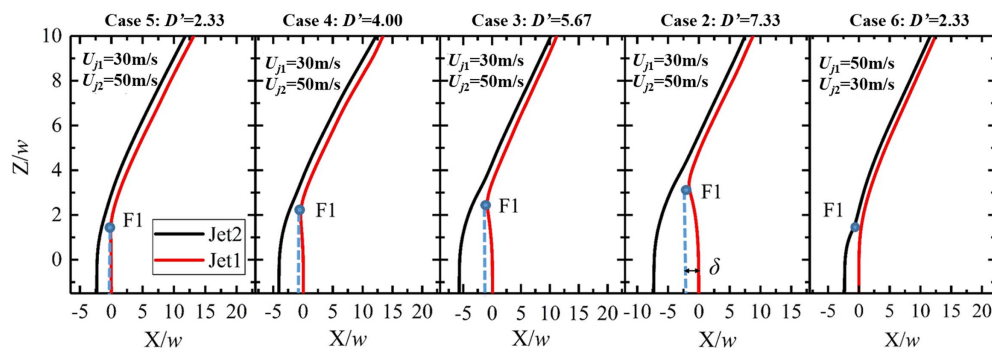

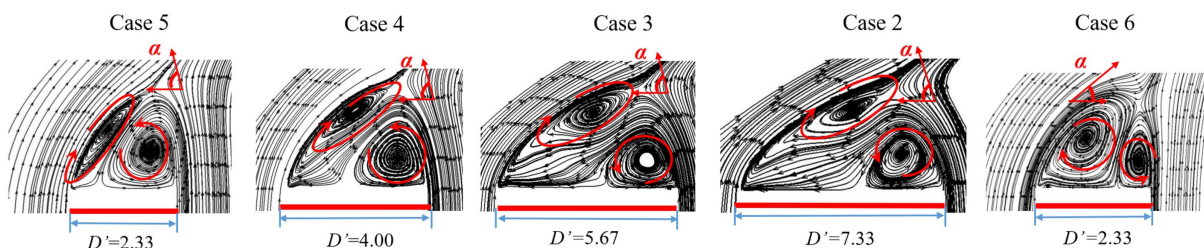**Fig. 13.** Trajectory curve of the tandem jets.
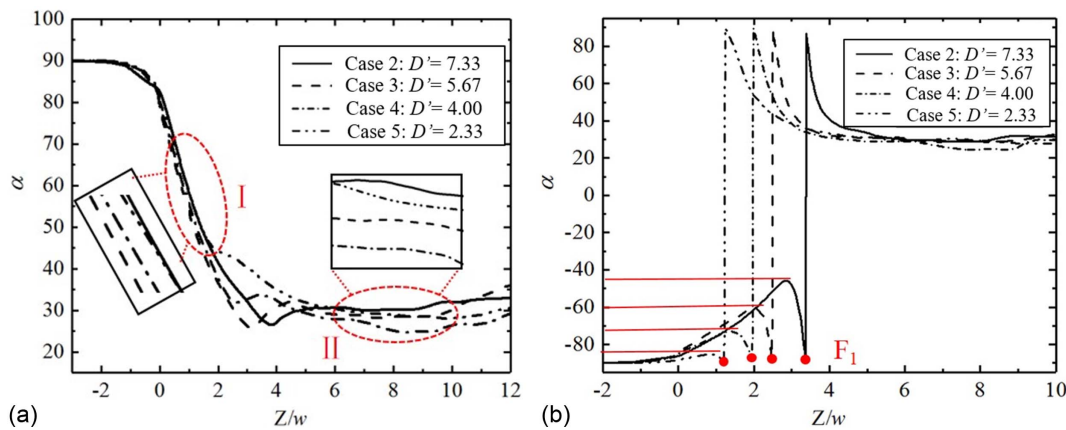

Fig. 14. Vortex distribution in S_D.

Fig. 15. Tangential angle α of the tandem jets: (a) upstream jet; and (b) downstream jet.

the maximum change of tangential angle $\Delta\alpha_{max}$ increases linearly, and the offset δ increases exponentially.

Effect of Downstream Jet

In the last section of the trajectory study, it was found that due to the influence of the counterrotating vortex pair in the interaction area, the downstream jet trajectory was deflected, resulting in the change of the tangential angle of the downstream jet trajectory. To further understand the mechanism of the influence of the flow in the S_D region on the downstream jet trajectory, the downstream jet was further analyzed.

Fig. 17 is the streamline distribution, where Figs. 17(a and b) are the streamline distribution of different D'. Flow Parts 1, 2, and 3 represent different flow directions. In addition, Fig. 17(c) is the boundary of Flow Parts 1, 2, and 3, the contour line without arrow

is the velocity contour in the Z-direction, and o, p, and q are the percentage of the flow area of each part in the total width of the downstream jet. First, it can be seen from Fig. 17 that the formation of R_1 and R_2 is related to the shearing effect of the upstream and downstream jet, and the flow of the downstream jet is divided into multiple flow directions due to the adsorption effect of R_2. Second, when $D' = 2.33$, the flow of the downstream jet is mainly composed of Parts 1 and 3, most of Flow 3 is injected vertically. Finally, it can also be found that with the increase of D', the flow of the downstream jet is divided into three parts. Flow Part 1 is related to the formation of the vortex R_2, and another Part 2 is mixed with the shear layer of the upstream jet and accelerated, which inhibits the upstream jet from forming the vortex R_1. Therefore, Flow Part 2 became the main source of R_1. The flow direction of Flow Part 3 remains vertical.

Fig. 18 shows the percentage of each flow part of the downstream jet, where 1, 2, and 3 correspond to o, p, and q, respectively.

Table 3. Value of maximum deflection angle and offset of the downstream jet with D

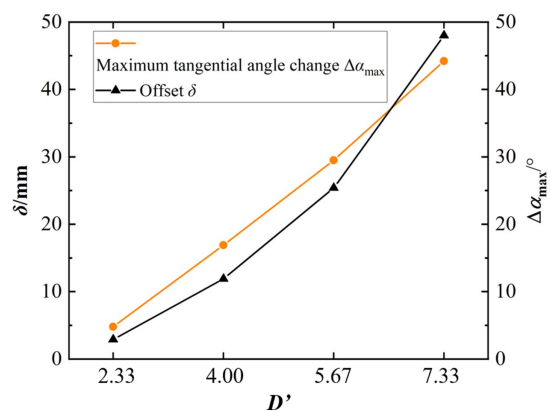| D'	$\Delta\alpha_{max}$ (degrees)	Offset δ (mm)
2.33	4.8	2.9
4	16.9	11.9
5.67	29.5	25.4
7.33	44.2	48

Fig. 16. Variation of maximum deflection angle and offset the downstream jet with D'.
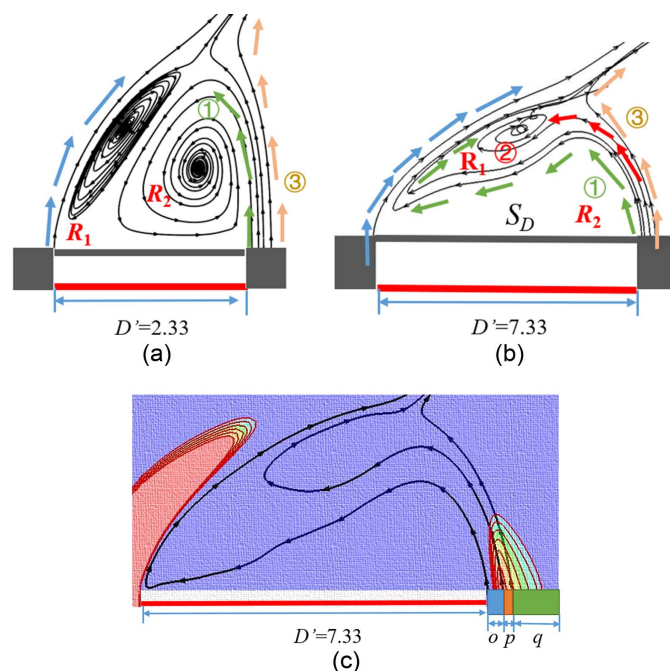

Fig. 17. Streamline distribution of different D': (a and b) streamline distribution; and (c) boundary of flow parts.
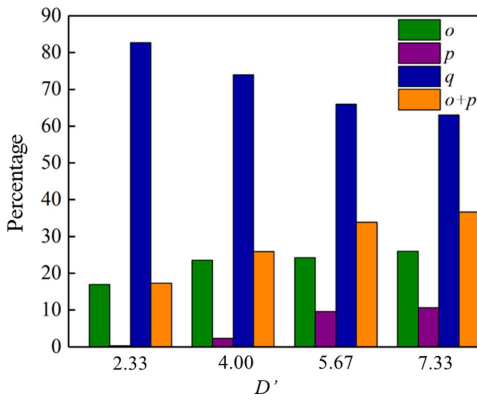
Fig. 18. Percentage of each flow part.

It can be seen from Fig. 18 that with the increase of the spacing D, the proportion of Flow regions 1 and 2 increases, and most of the flow in 1 is accelerated by the upstream jet and mixed with the downstream jet. In addition, with the increase of D', the interaction zone S_D between the jets becomes larger, and the proportion of 1 and 2 increases so the S_D area can be effectively filled, but when D' increases to 7.33, the proportion of 1 and 2 increases less; as a result, the S_D area's inadequate packing makes the flow in this area more unstable, thus causing the downstream jet swinging before mixing, which makes the offset of the downstream jet increase significantly when D' is 7.33.

Time-Averaged Velocity Distributions on the Trajectories

To further understand the flow characteristics on the trajectories, it is helpful to further discuss the time-averaged velocity distributions on the trajectories, which are shown in Figs. 19 and 20. The U_x

and U_z are the velocity components in the horizontal and vertical directions, and U is the resultant velocity.

It can be seen from Fig. 19 that U_x increases rapidly first and then suddenly decreases. In particular, in the absence of the downstream jet, the U_x reduction is faster. Additionally, for the single jet, U_z gradually decreases and drops to zero. However, for the tandem jets, the U_z value of the upstream jet increases and tends to a stable value.

In Fig. 20, it is apparent that the downstream jet has a negative value of U_x due to the adsorption of the vortices R_2, and as D' increases, the velocity U_x increases in the negative direction and U_z decreases. Then, after reaching the peak, U_x increases in the opposite direction, and U_z continues to decrease for Case 5 ($D' = 2.33$) and Case 4 ($D' = 4.00$). When $D' > 5.67$, U_z increases slightly. For the case with the same spacing D and the upstream and downstream jet velocities are reversed (i.e., Cases 1 and 6), time-averaged velocity distribution rules of the jet trajectories are also reversed.

In general, the time-averaged velocity distributions on the jet trajectories of single jet and tandem jets are obviously different. For the tandem jets, the time-averaged velocity along the trajectory changes regularly with the change of the spacing D'. At the same time, when the jets' velocity change (i.e., the upstream and downstream jet velocities are reversed), the time-averaged velocity distribution jet trajectories are also reversed.

Penetration Variation against Trajectory

Jet penetration into incoming flow is an important feature of S/TJICF. In this process, some complex flow phenomena, such as entrainment and vortex generation, occur between jets and incoming flow due to shear effect. Therefore, study of penetration can contribute to a deep understanding of the complex flow of J/TICF. The trajectory can be used to approximately describe the penetration depth, but it can only describe the change of the jet center
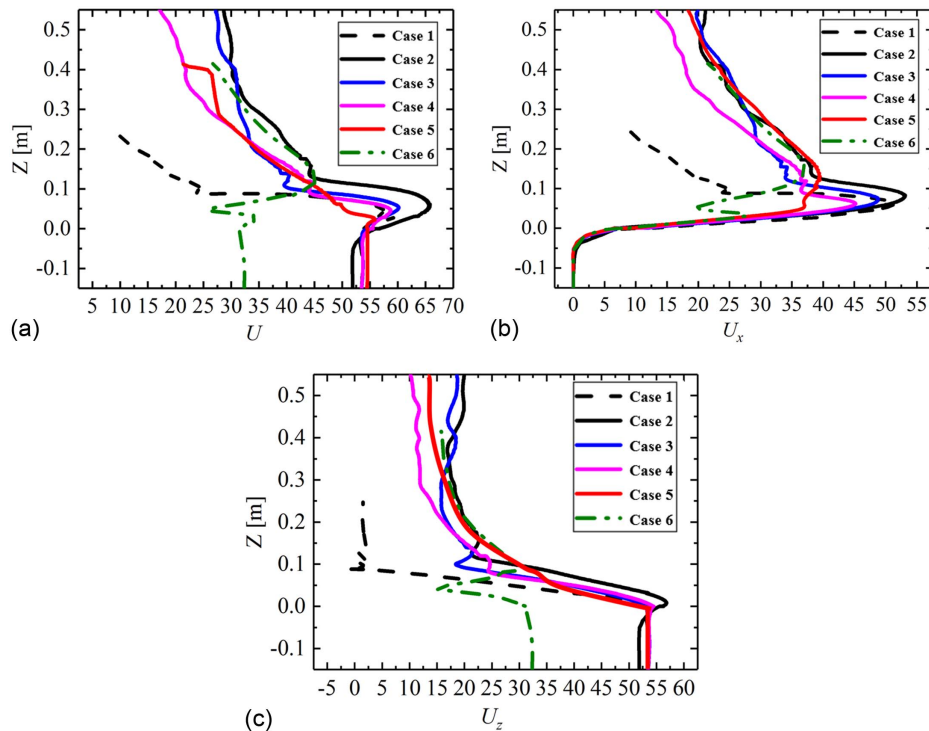

Fig. 19. Velocity distributions on the trajectories of the upstream jet.
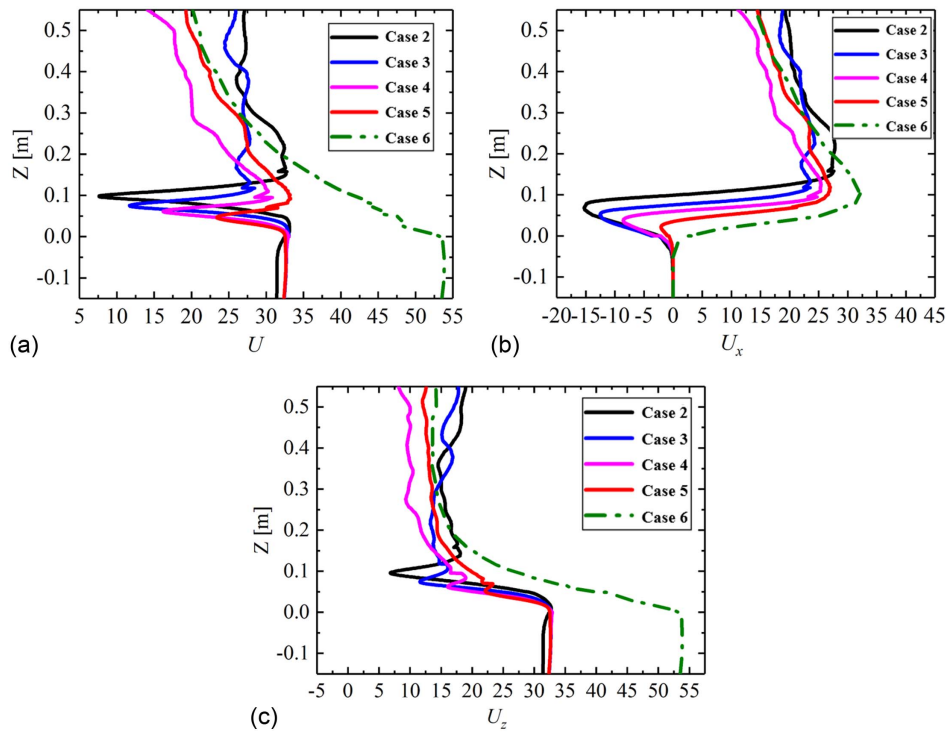
Fig. 20. Velocity distributions on the trajectories of the downstream jet.

trajectory and cannot clearly describe the penetration boundary. However, when analyzing penetration variation against trajectory, they are positively correlated, and as such a corresponding study can be conducted.

The contour of velocity magnitude cannot clearly analyze the penetration and mixing of jets, especially for multijet problems. Instead, researchers (Ivanova et al. 2010; Ryan et al. 2017) use an ST model to analyze the mixing of the jets and cross flow, which was also used in this paper, and the distribution of jet penetrating the incoming flow can be clearly seen.

Scalar Transport Model

The transport equation for a passive scalar is

$$\frac{\partial}{\partial t}(\rho Y_i) + \nabla \cdot (\rho \mathbf{u} Y_i) = -\nabla \mathbf{J}_i \tag{8}$$

where $\mathbf{J}_i$ = diffusion flux of species i; and parameter Y_i = mass fraction of species i. The passive scalar Y_i is used to calculate the mass fraction distribution of the jet, and the variation range of Y_i is 0–1, where 1 and 0 represent that the mass fraction of the jet is 100% and 0%, respectively (Ivanova et al. 2010; Ryan et al. 2017). As such, the Y_i value of the jet should be 1 and the Y_i value of the incoming flow should be 0. Furthermore, for tandem jets, owing to the different velocities of the two jets, the amount of flow ingested is different. The value of Y_i is distributed according to the velocity ratio of the jet, such as $U_{j1}/U_{j2} = 3/5 = Y_{j1}/Y_{j2}$, and $Y_{j1} + Y_{j2} = 1$. After solving the scalar transport model, the distribution of mass fraction will be obtained, so the jet penetration can be assessed more clearly and intuitively according to the contour of the mass fraction. This study mainly used the time-averaged mass fraction distribution to analyze the penetration characteristics of the jets.

We adopted the ST method to describe the penetration characteristics of a jet based on the results of a scalar transport model.

Fig. 21 shows the time-averaged mass fraction C_{mass} distribution of the jets, where Fig. 21(a) shows the substance concentration C_{mass} distribution of the single and tandem jets, and the filtered C_{mass} range is 0.25–0.8. Fig. 21(b) shows the time-averaged mass fraction distribution of the single jet. It can be seen from Fig. 21(a) that the area where $C_{mass} = 0.25$–0.8 is the main area for jet and incoming flow mixing, and it can be observed that the penetration depth of tandem jets is significantly higher than that of a single jet. Moreover, this area also clearly shows the penetration boundary after the jet penetrates the crossflow. To obtain the penetration boundary, the contour line of $C_{mass} = 0.26$ was selected as the penetration boundary line [as shown in the dotted line diagram in Fig. 21(a)].

Penetration Boundary and Trajectories

The mass fraction distribution of the jet can be obtained using the scalar transport model, and the penetration boundary formed after mixing the jet with the incoming flow can be described quantitatively. This study focused on the impact of different cases on the penetration, such as single/tandem jets and tandem jets with different spacing D'.

Fig. 22 shows the mass fraction C_{mass} distribution of the tandem jets for the constant velocity, and the D' changes of Cases 2–5 corresponding to Figs. 22(a–d). It can be seen from Fig. 22 that the height of the air curtain formed by tandem jets is higher than that of the single jet, and the width of the jet area formed increases slightly with the increase of D'. Then the two jets mix, and the concentration in the S_D area decreases with the increase of D'.

According to the method of Fig. 22(a), the penetration boundary curve is selected to describe the penetration depth as shown in Fig. 24. Fig. 24(a) shows the penetration characteristic curves of Cases 1–5. The ΔS and ΔT are the penetration depth corresponding to Cases 1 and 4, respectively, and their ratio is shown using the
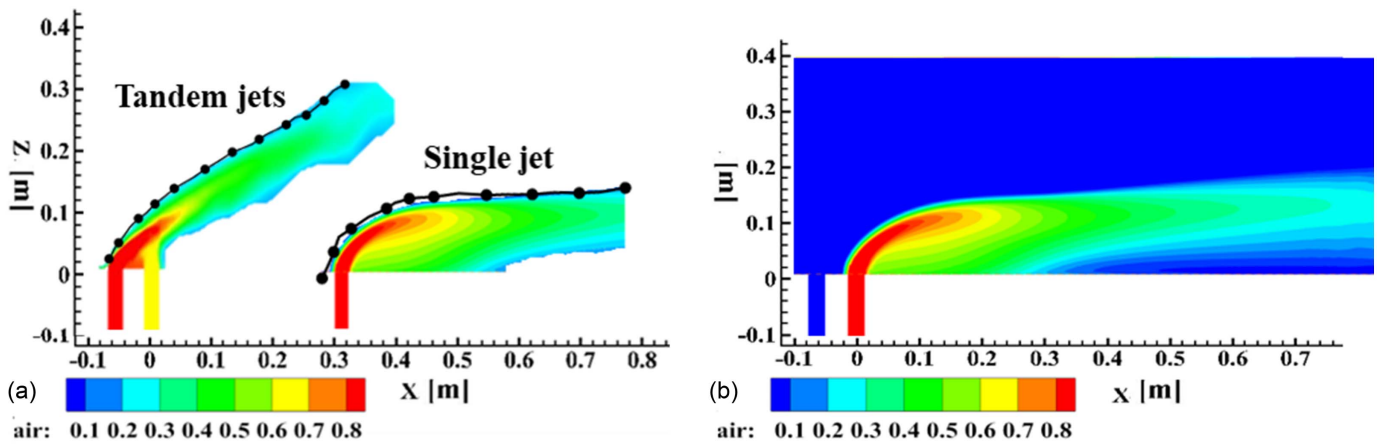
Fig. 21. Time-averaged mass fraction C_{mass} distribution: (a) filtered C_{mass} of single and tandem jets; and (b) C_{mass} distribution of the single jet.

line with triangle in Fig. 24(b). At the same time, the ratio $\Delta T/\Delta S$ of the trajectory height of single and tandem jets is plotted using the same method is shown by the line with square in Fig. 24(b). At the same time, the changes of the penetration boundary curve and the upstream jet trajectory are compared, as shown in Fig. 23.

First, combining Figs. 22 and 23, it is found that for the single jet, owing to its large mixing zone (i.e., concentrated distribution area of jets' mass fraction), the difference between the central trajectory curve and the penetration boundary curve is large, and ΔZ can reach 59.3 mm. Second, for the tandem jets, the mixing zone between the jets and the incoming flow is obviously narrowed and relatively concentrated, and the difference between the penetration boundary curve and the trajectory curve decreases, and the

difference will also increase with the increase of the D'. Moreover, for $D' = 4.00$, the difference between the penetration boundary curve and the trajectory curve is obviously greater than other cases; ΔX can reach 133.8 mm at most.

By analyzing Fig. 24, on the one hand, it can be concluded that the penetration depth of the single jet is slightly higher than that of tandem jets when $0 < X/w < 1$. On the other hand, when $X/w > 1$, the penetration depth of the upstream jet in the tandem jet configuration is much higher than that of the single jet. In addition, for comparison between penetration curve and trajectory line, when the penetration depth reaches the maximum, the corresponding D' is 4.00, while when the trajectories are the highest, the corresponding D' is 2.33. More importantly, the maximum
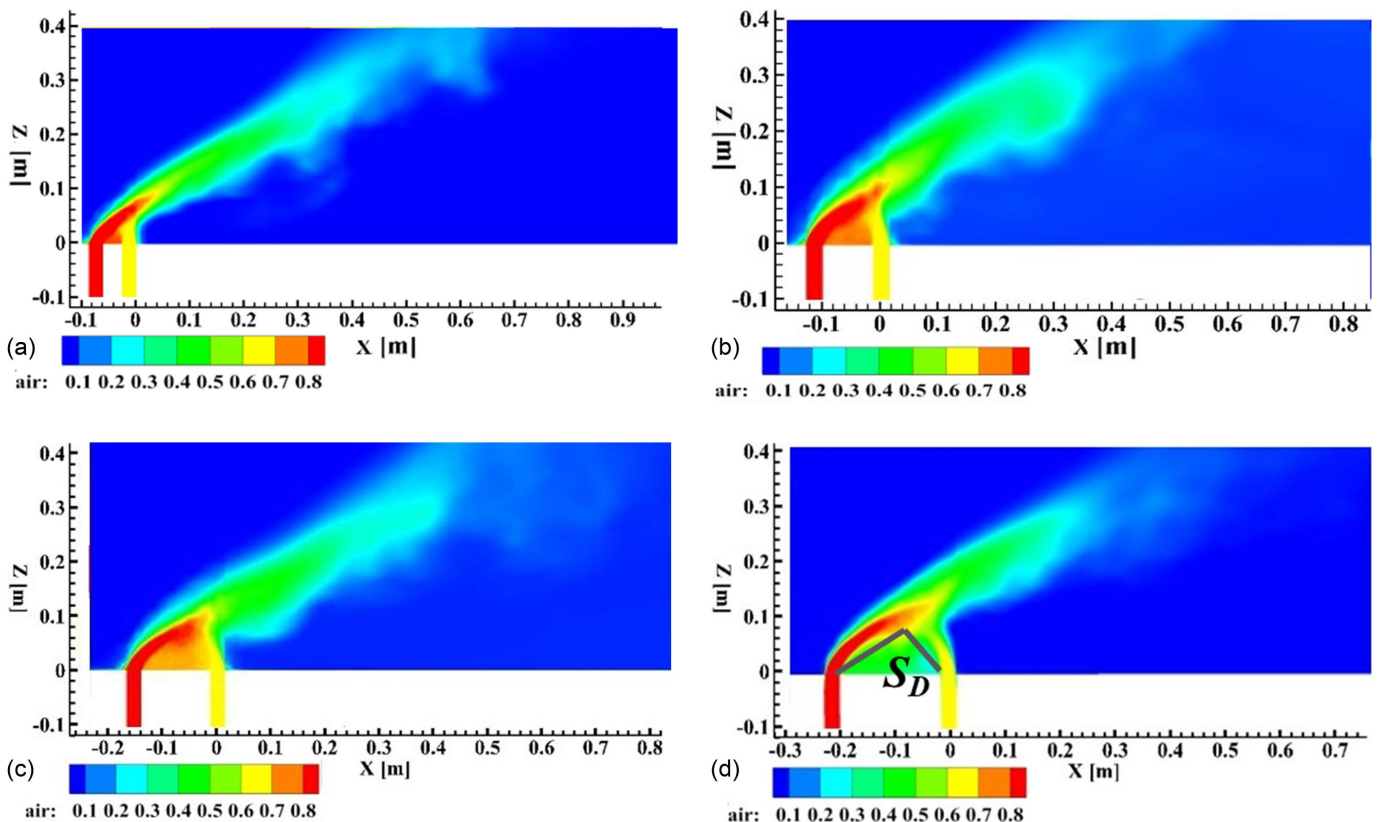

Fig. 22. Mass fraction distribution ($C_{mass} = 0–0.8$): (a) Case 5; (b) Case 4; (c) Case 3; and (d) Case 2.
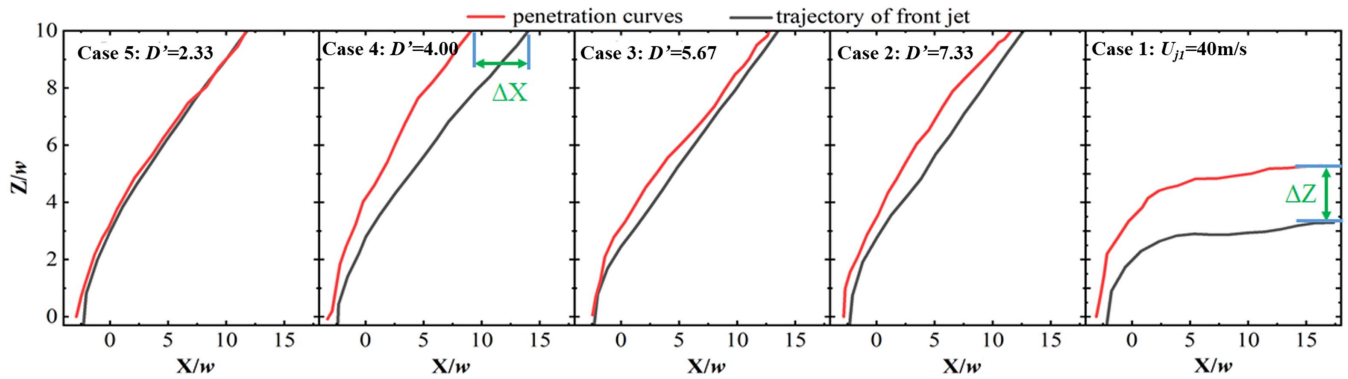
Fig. 23. Comparison of penetration boundary curve and upstream jet trajectory.
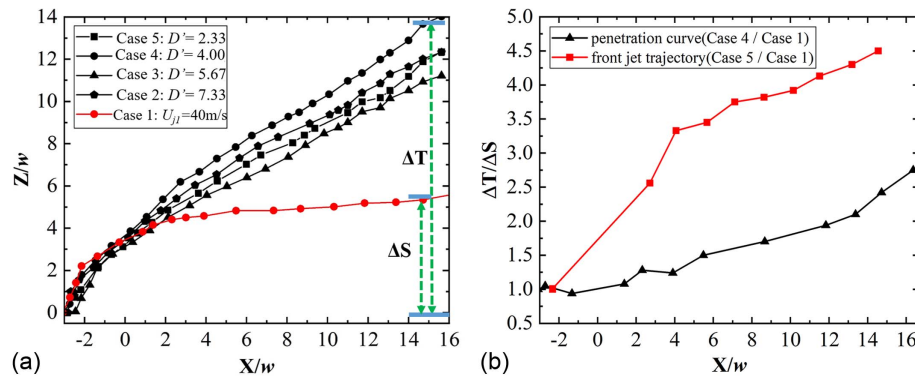

Fig. 24. Penetration characteristic curves: (a) penetration characteristic curves of Cases 1–5; and (b) $\Delta T / \Delta S$ for penetration and trajectory.

ratio $\Delta T / \Delta S$ of the penetration depth of single and tandem jets can reach 2.8, while the maximum ratio $\Delta T / \Delta S$ of the trajectories can reach 4.5.

In general, the height of the penetration boundary curve is always higher than the height of the trajectory. When $D' = 2.33$, the difference between the penetration boundary curve and the trajectory is the smallest. As the spacing D' increases, the difference increases first and then decreases. When $D' = 4.00$, the difference reaches the maximum.

Interaction of the Jets Associated with the Trajectory

Interaction of the jets is an important and complicated feature in TJICF. In this paper, the analysis of the interaction was conducted from the spectral analysis point of view.

PSD Analysis
The PSD function is an important tool for flow stability analysis and is often used to study the stability and frequency characteristics of a shear layer (Pokharel and Acharya 2021). Data from different points in the flow area are selected to perform PSD analysis on the fluctuation velocity. The sampling time step is 1.25×10^{-4} s, making the maximum sampling frequency 8,000 Hz. According to the Nyquist theorem, the analysis frequency can be up to 3,200 Hz. The Welch's method is used to calculate the power spectrum. The block size is 2^{11}, and the overlapping length between each window is 50%. The Hanning window function is used.

Fig. 25 is a schematic diagram of the selected points, in which Q_1 and Q_2 are points respectively close to the upstream and downstream jets. Points P1–P4 are equidistant points in the center of the

upstream and downstream jet trajectory, which are mainly used to analyze fluctuations of the tandem jets after mixing.

Fig. 26 is the PSD diagrams of the vertical velocity of Q_1, Q_2, and a certain point Pi in the central area under different spacing, and the frequencies corresponding to the peaks as given in Table 4. Fig. 27 is the PSD diagram at Points P1 to P4.

Based on the analysis of Figs. 26 and 27 and Table 4, it can be first concluded that as the spacing increases, the center frequency f_c decreases. When $D' = 2.33$, the upstream jet fluctuation frequency f_a is about 314 Hz, the downstream jet fluctuation frequency f_b is 82.1 Hz, and the central area fluctuation frequency f_c tends to be closer to the upstream jet fluctuation. The frequencies
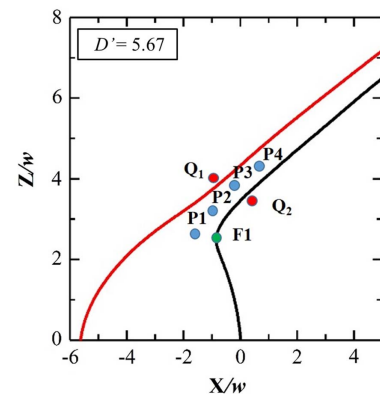

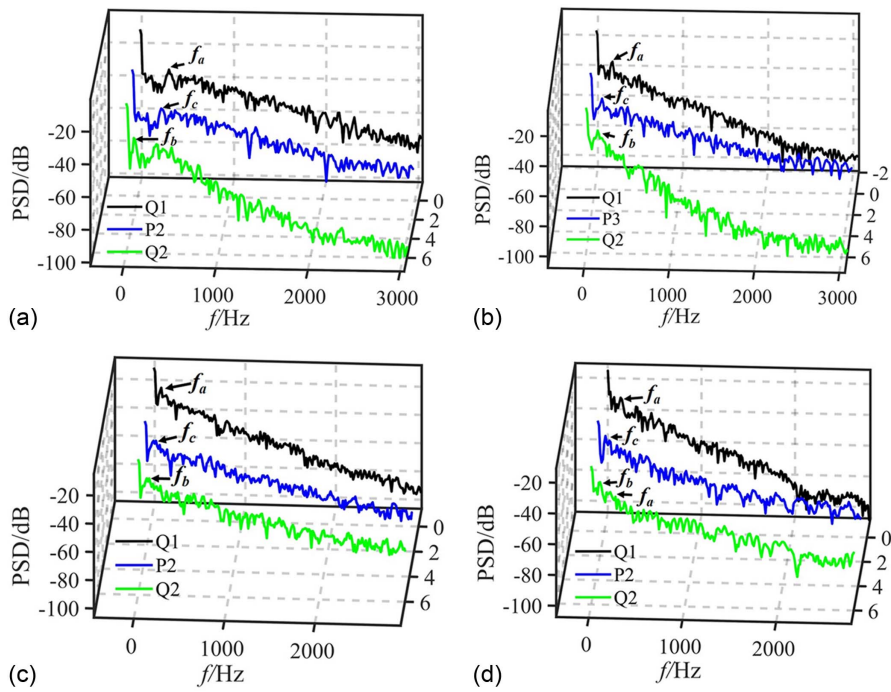**Fig. 25.** Schematic diagram of the selected points.

Fig. 26. PSD diagrams of the vertical velocity at Q_1, Q_2, and Pi: (a) Case 5; (b) Case 4; (c) Case 3; and (d) Case 2.

Table 4. Frequency corresponding to peak value at Q_1, Q_2, and Pi

Frequency	$D' = 2.33$	$D' = 4.00$	$D' = 5.67$	$D' = 7.33$
f_a	314.4	191.4	82.3	150.4
f_c	314.4	136.7	95.7	82.0
f_b	82.1	136.7	95.7	82.0

f_a and f_c are the same, indicating there is no obvious mixing effect between the upstream and downstream jets. In addition, when $D' = 4.00$, f_a decreases and f_b increases, indicating that the two jets are mixed to affect their velocity fluctuations. The fluctuation frequency f_c in the central area is consistent with f_b. Then, when $D' = 5.67$, the fluctuation frequencies of f_a and f_b are both
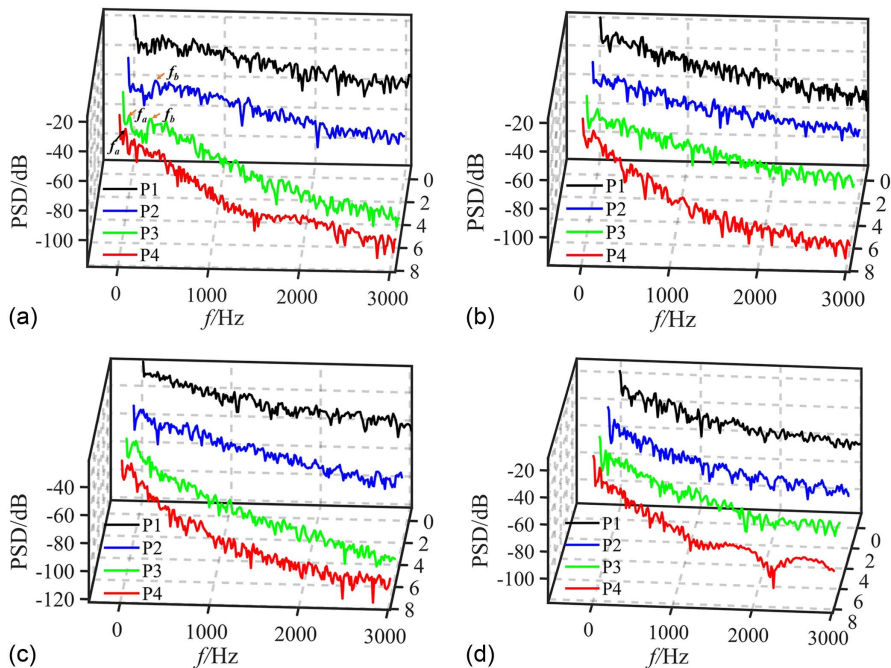

Fig. 27. PSD diagrams of the vertical velocity at P1–P4: (a) Case 5; (b) Case 4; (c) Case 3; and (d) Case 2.

decreased and the difference is not significant, indicating that the two jets are sufficiently mixed and the flow after mixing is relatively stable. Finally, when $D' = 7.33$ and the fluctuation frequency of f_a increases again, the fluctuation frequency f_b is consistent with the case of $D' = 2.33$. In general, through comprehensive analysis, it was found that when $D' = 5.67$, the frequencies f_a, f_b, and f_c have the smallest difference, indicating that the flow after mixing is more stable in this state.

SPOD Modal Analysis

Some researchers (Zhao et al. 2018b) used the proper orthogonal decomposition (POD) method to analyze the mode of tandem jets, but it cannot represent the time evolution of the structure (Towne et al. 2018). The SPOD method is evolved from POD, which was originally derived by Lumley (2007) according to the stochastic method. The POD method often used the velocity variable $v(x, t)$ in the flow field, which is related to time and space, and it looks for a certain function $\Phi(x)$ to better approximate this random variable. First, we need to find a correlation function of time and space

$$R(x, x', t, t') = \langle v_k(x, t) v_k^*(x', t,) \rangle \qquad (9)$$

where $\langle \rangle$ is used to find the ensemble average of $v(x, t)$; and v_k and v_k^* are any two adjacent points. From the correlation function R, the POD mode $\Phi(x)$ can be obtained by solving the Lumley integral formula

$$\iint R(x, x', t, t') \Phi_k(x', t') dx' dt' = \lambda_k \Phi_k(x, t) \qquad (10)$$

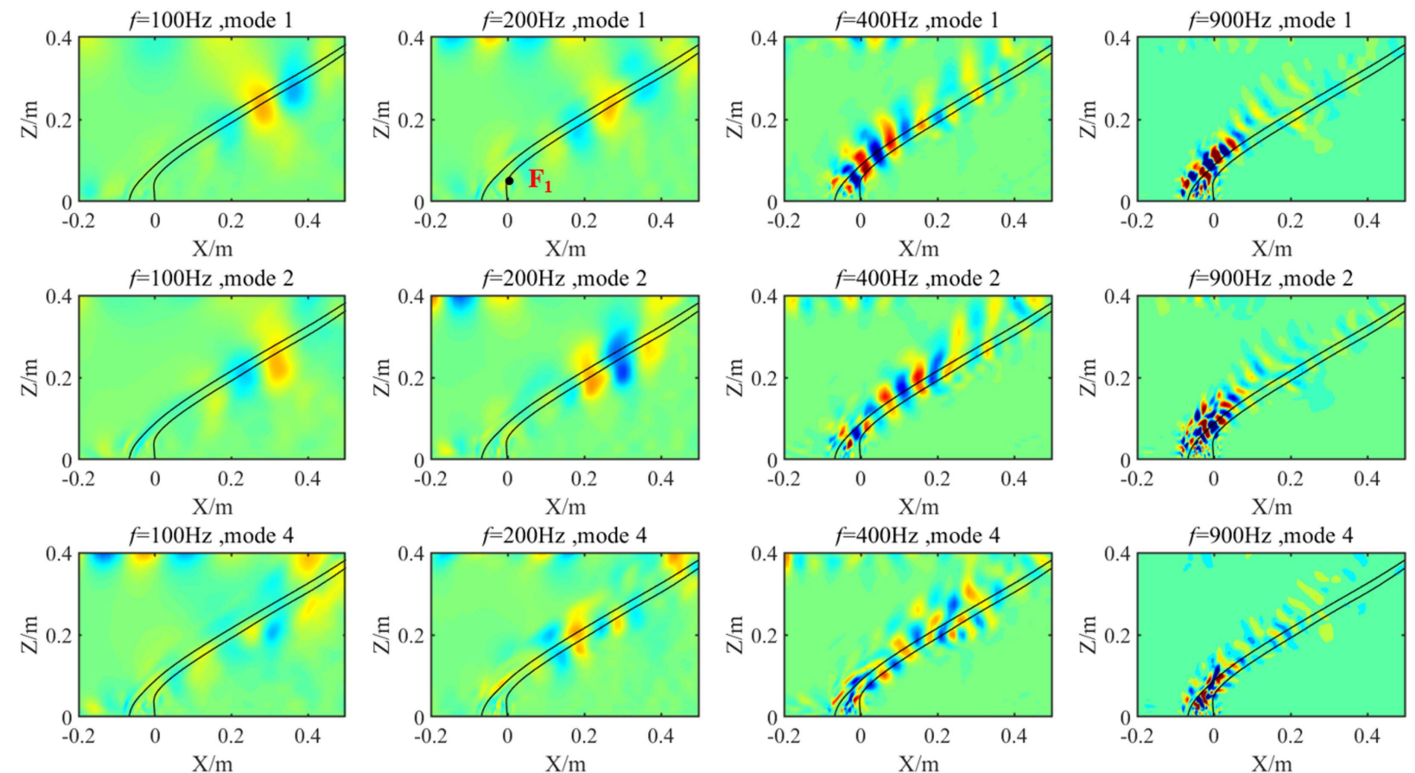Through eigenvalue decomposition, the obtained POD modes decompose the flow

$$v_j(x, t) = \sum_k \alpha_{jk} \Phi_k(x, t) \qquad (11)$$

For SPOD, the conversion from the time domain to the frequency domain is carried out on the basis of POD, so as to obtain the time correlation of long time series (Towne et al. 2018). First, a segment time scale τ is introduced, and a window function $w(\tau) = e^{(-(\tau/T)2)}$ is set on the total time scale T. The spatiotemporal correlation function becomes

$$R(x, x', t, t') = \langle v_k(x, t + \tau) w(\tau) v_k^*(x', t + \tau') w * (\tau')) \rangle \qquad (12)$$

$$\iint R(x, x', \tau, \tau') \Phi_k(x', \tau') dx' d\tau' = \lambda_k \Phi_k(x, \tau) \qquad (13)$$

The modal analysis of the vertical velocity component U_z on the central section of TJICF was carried out using the SPOD method. Figs. 28–30 show the SPOD modal distribution of the velocity component U_z for $D' = 2.33$, 5.67, and 7.33, respectively.

First, based on the PSD analysis results, it was found that the main frequency fluctuations at $D' = 2.33$ are $f_a = f_c = 314.2$ Hz. Therefore, in the SPOD results from Fig. 28, it was found that under $f = 100$ and 200 Hz, except for the area where the trajectory line $Z > 0.2$ m, there are few fluctuation structures. Meanwhile, when $f = 400$ Hz, Modes 1 and 2 show coherent structures that are uniformly distributed along the trajectory, and the coherent structures are mainly biased toward the distribution of the upstream jet trajectory, indicating that the central area is greatly affected by the upstream jet.

Second, as can be seen in Fig. 29, it can be concluded that with the increase of D', the fluctuation frequency f_c decreases, resulting in a few coherent structures appearing at low frequencies ($f = 80$, 160 Hz). Furthermore, when $f > 400$ Hz, the coherent structures
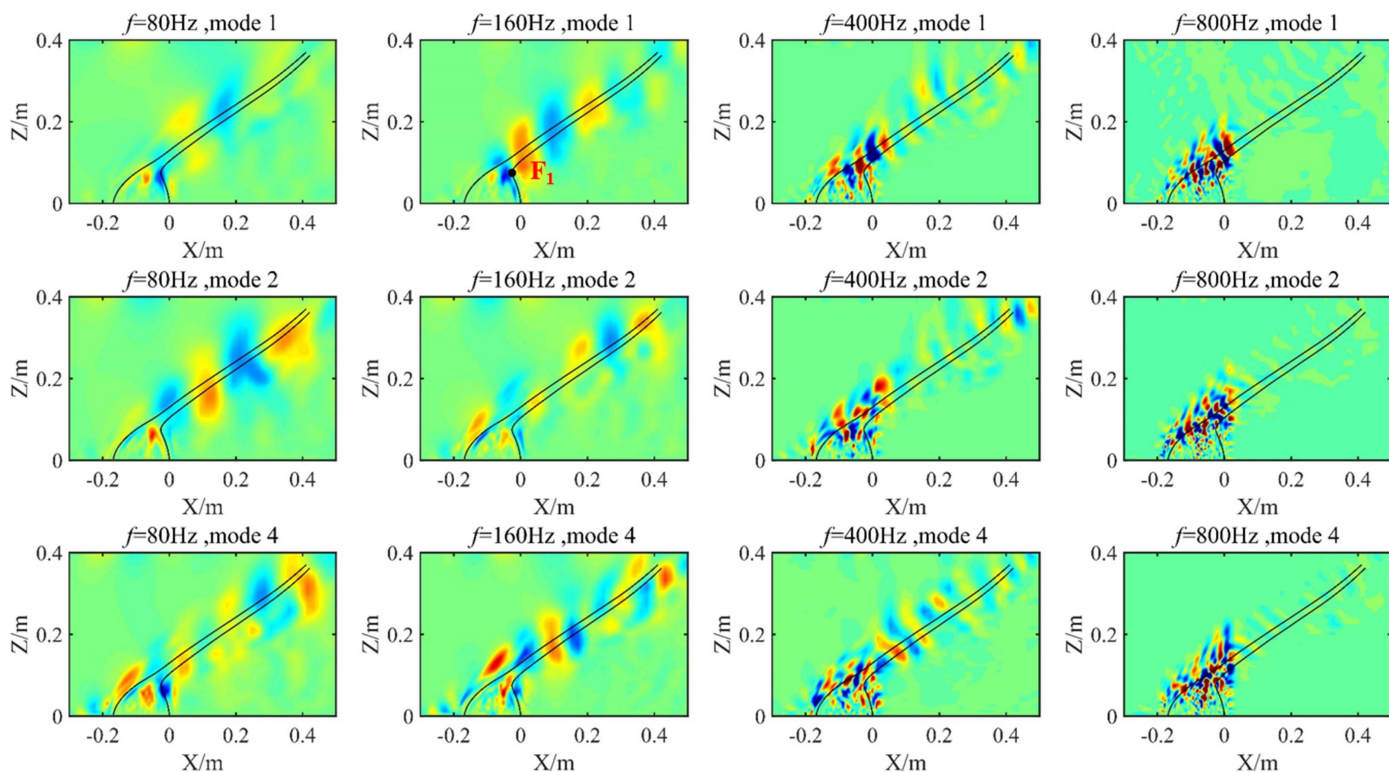

Fig. 28. SPOD modal distribution ($D' = 2.33$).

Fig. 29. SPOD modal distribution ($D' = 5.67$).
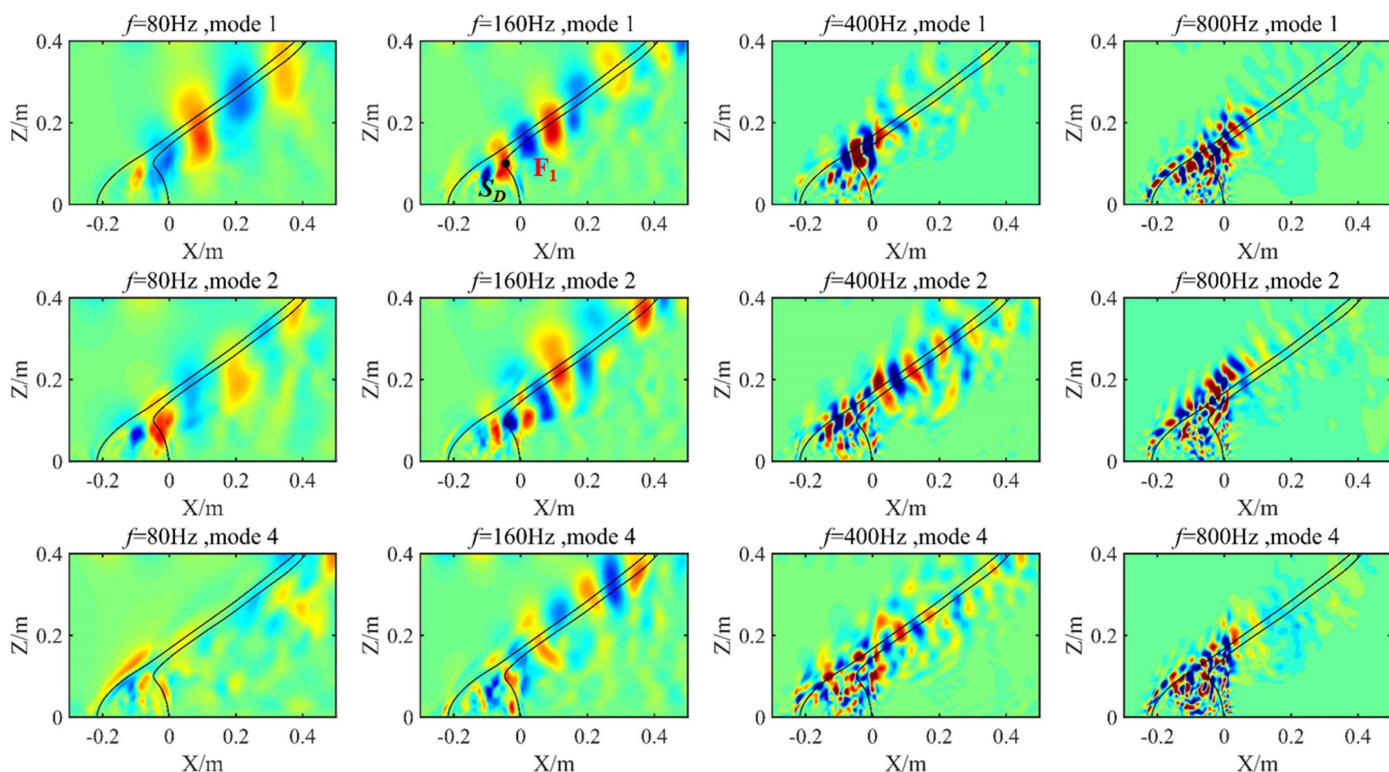
Fig. 30. SPOD modal distribution ($D' = 7.33$).

around the trajectory curves in the region of $Z > F_1$ are significantly reduced compared with $D' = 2.33$ and 7.33, and combined with the PSD results, the difference between the fluctuation frequencies f_a and f_b is the smallest in this case, indicating once

again that the upstream and downstream jets are thoroughly mixed during the flow process, making the flow most stable.

What is more, it can be seen from Fig. 30 that compared with $D' = 5.67$, there is a significant increase in coherent structures,

indicating that the flow fluctuation is strengthened, and the flow is unstable. Moreover, many small coherent structures are decomposed in the S_D area, and the coherent structures in the S_D area are the most obvious at $D' = 7.33$. Combined with the analysis of the PSD analysis, it is concluded that the S_D area is not effectively filled due to the large spacing, which makes the flow in this area more prone to fluctuations, resulting in flow instability.

Conclusion

This paper performed an LES numerical simulation to study the trajectory, as well as the penetration and interaction of S/TJICF related to the jet trajectory. To begin with, the simulation model was validated by experiments. Then the flow characteristics associated with trajectories, e.g., the variation and modeling, and the penetration depth of the jet using scalar transport were analyzed. Furthermore, PSD and SPOD were used to study the interaction of the jets. The following important conclusions can be drawn:

- Through modeling and characteristic analysis (e.g., velocity, tangential angle) of the trajectories, it is found that the height of the trajectory curves of the tandem jets is significantly higher than that of the single jet. In addition, the upstream jet trajectory changes little at different spacing D', while the downstream jet deflects as a result of the influence of the counterrotating vortex pair in the S_D area. Moreover, the S_D area is not effectively filled with the increase of D', which causes the downstream jet to fluctuate, thus causing a greater deflection of the downstream jet trajectory.
- Based on the scalar transport model, the penetration characteristics of S/TJICF and the variation characteristics of the penetration boundary curves were analyzed and the trajectories were compared. It was found that the height of the penetration boundary curve is always higher than the height of the trajectory. When $D' = 2.33$, the difference between the penetration boundary curve and the trajectory is the smallest. As the spacing D' increases, the difference increases first and then decreases. When $D' = 4.00$, the difference reaches the maximum. In addition, the height of the trajectory formed by the tandem jets can reach four times that of the single jet, and the penetration depth of tandem jets can reach 2.8 times that of the single jet.
- The fluctuation frequencies of the upstream jet and the downstream jet are different due to the different velocities. When $D' = 2.33$, the fluctuation of the central area is significantly affected by the upstream jet fluctuation, and the jet frequency difference between upstream and downstream is quite large, indicating that the mixing of the tandem jets is poor. In addition, with the increase of D', the fluctuation frequency of the central area is consistent with the downstream jet. Moreover, when $D' = 5.67$, the fluctuation frequency of the tandem jets decreases and the difference is the smallest, indicating that the two jets are fully mixed, and the flow is the most stable.
- When the spacing is small, the coherent structures are inclined to the distribution of the upstream jet trajectory, the fluctuation frequency after mixing is dominated by the upstream jet, and the frequency is high. However, with the increase of D', the fluctuation frequency decreases, and the coherent structures begin to appear at low frequencies. At the same time, the coherent structures are mainly distributed evenly along tandem jets, and the fluctuation frequency is greatly affected by the downstream jet. Furthermore, when $D' = 5.67$, the frequency difference between the upstream and downstream jets is minimal, and the coherent structures are significantly reduced, indicating that the flow mixing is the best and the mixed flow is the most stable.

On the other hand, when $D' = 7.33$, the coherent structures generated in the area S_D are the most obvious, which makes the flow stability worse after the jets and the incoming flow are mixed.

Data Availability Statement

Some or all data, models, or code that support the findings of this study are available from the corresponding author upon reasonable request.

Acknowledgments

Notation

The following symbols are used in this paper:

A, B, C = correlation coefficients;
C_{mass} = time-averaged mass fraction distribution of the jets;
D = distance between the centers of the two jets;
$D' = D/w$, by dimensionless D of w;
$\mathbf{J}_i$ = diffusion flux of species i;
$\bar{p}$ = pressure of the fluid;
q = momentum ratio;
R_1, R_2 = two counterrotating vortex pairs;
$R(x, x', t, t')$ = correlation functions;
S_D = interaction zone between the two jets;
$\bar{S}_{ij}$ = strain tensor;
U_{j1} = velocity of the upstream jet;
U_{j2} = velocity of the downstream jet;
$\bar{u}_i$ = velocity component;
w = nozzle width;
$w(\tau) = e^{(-(\tau/T)^2)}$ = window function;
Y_i = mass fraction of species i;
α = tangential angle of the trajectory;
$\Delta\alpha_{\text{max}}$ = tangential angle change;
δ = maximum offset at the inflection point F_1;
ν = viscosity;
v_k, v_k^* = any two adjacent points;
$\boldsymbol{\nu}_{sgs}$ = eddy viscosity model;
ρ = density of the fluid;
τ = segment time scale;
τ_{ij} = compressive lattice stress;
$\Phi_k(x', t')$ = POD mode $\Phi(x)$; and
$\langle\rangle$ = used to find the ensemble average of $v(x, t)$.

References

Acharya, S., M. Tyagi, and A. Hoda. 2006. "Flow and heat transfer predictions for film cooling." *Ann. N. Y. Acad. Sci.* 934 (1): 110–125. https://doi.org/10.1111/j.1749-6632.2001.tb05846.x.

Fearn, R., and R. P. Weston. 1974. "Vorticity associated with a jet in a cross flow." *AIAA J.* 12 (12): 1666–1671. https://doi.org/10.2514/3.49576.

Ghenai, C., H. Sapmaz, and C.-X. Lin. 2009. "Penetration height correlations for non-aerated and aerated transverse liquid jets in supersonic cross flow." *Exp. Fluids* 46 (1): 121–129. https://doi.org/10.1007/s00348-008-0547-8.

Gutmark, E. J., I. M. Ibrahim, and S. Murugappan. 2008. "Circular and noncircular subsonic jets in cross flow." *Phys. Fluids* 20 (7): 075110. https://doi.org/10.1063/1.2946444.

Gutmark, E. J., I. M. Ibrahim, and S. Murugappan. 2011. "Dynamics of single and twin circular jets in cross flow." *Exp. Fluids* 50 (3): 653–663. https://doi.org/10.1007/s00348-010-0965-2.

Haniu, H., and B. R. Ramaprian. 1989. "Studies on two-dimensional curved nonbuoyant jets in cross flow." *J. Fluids Eng.* 111 (1): 78. https://doi.org/10.1115/1.3243603.

Huang, R. F., and C. I. Chou. 2009. "Flow and performance of an air-curtain biological safety cabinet." *Ann. Occup. Hyg.* 53 (4): 425–440. https://doi.org/10.1093/annhyg/mep020.

Isaac, K. M. 1982. "Experimental and analytical investigation of multiple jets in a cross-flow." Doctoral thesis. Dept. of Aerospace Engineering, Virginia Tech and State Univ.

Isaac, K. M., and A. K. Jakubowski. 1985. "Experimental study of the interaction of multiple jets with a cross flow." *AIAA J.* 23 (11): 1679–1683. https://doi.org/10.2514/3.9151.

Ivanova, E., B. Noll, and M. Aigner. 2010. "Unsteady simulations of turbulent mixing in jet in crossflow." In *Proc., 40th Fluid Dynamics Conf. Exhibit*. Reston, VA: American Institute of Aeronautics and Astronautics.

Kiel, B., C. Murawski, S. Gogineni, A. Cox, and M. Flanagan. 2003. "Experimental investigation of vortex shedding of a jet in crossflow." In *Proc., 41st Aerospace Sciences Meeting and Exhibit Conf.*, Reston, VA: American Institute of Aeronautics and Astronautics.

Kumar, P. A., S. B. Verma, and S. Elangovan. 2011. "Study of jets from rectangular nozzles with square grooves." *Aeronaut. J.* 115 (1165): 187–196. https://doi.org/10.1017/S0001924000005583.

Lai, A. C. H., and J. H. W. Lee. 2010. "Multiple tandem jet interaction in a crossflow." *J. Hydrodyn. Ser B* 22 (5): 639–643. https://doi.org/10.1016/S1001-6058(10)60007-8.

Lin, K.-C., P. Kennedy, and T. Jackson. 2002. "Penetration heights of liquid jets in high-speed crossflows." In *Proc., 41st Aerospace Sciences Meeting and Exhibit Conf.*, Reston, VA: American Institute of Aeronautics and Astronautics.

Lumley, J. L. 2007. *Stochastic tools in turbulence*. London: Academic Press.

Luo, N., A. G. Li, R. Gao, Z. G. Tian, W. Zhang, S. Mei, L. M. Feng, and P. F. Ma. 2013. "An experiment and simulation of smoke confinement and exhaust efficiency utilizing a modified opposite double-jet air curtain." *Saf. Sci.* 55 (Jun): 17–25. https://doi.org/10.1016/j.ssci.2012.12.002.

Makihata, T., and Y. Miyai. 1979. "Trajectories of single and double jets injected into a crossflow of arbitrary velocity distribution." *J. Fluids Eng.* 101 (2): 217. https://doi.org/10.1115/1.3448938.

New, T. H., and B. Zang. 2015. "On the trajectory scaling of tandem twin jets in cross-flow in close proximity." *Exp. Fluids* 56 (11): 1–12. https://doi.org/10.1007/s00348-015-2070-z.

No, S.-Y. 2015. "A review on empirical correlations for jet/spray trajectory of liquid jet in uniform cross flow." *Int. J. Spray Combust. Dyn.* 7 (4): 283–313. https://doi.org/10.1260/1756-8277.7.4.283.

Oerlemans, S., and A. C. Bruin. 2009. "Reduction of landing gear noise using an air curtain." In *Proc., 5th AIAACEAS Aeroacoustics Conf.* Reston, VA: American Institute of Aeronautics and Astronautics.

OlyaeiKebriaee, G., and A. Kebriaee. 2020. "Experimental study of liquid jets injected in crossflow." *Exp. Therm. Fluid Sci.* 115 (May): 110049. https://doi.org/10.1016/j.expthermflusci.2020.110049.

Pokharel, P., and S. Acharya. 2021. "Dynamics of circular and rectangular jets in crossflow." *Comput. Fluids* 230 (Mar): 105111. https://doi.org/10.1016/j.compfluid.2021.105111.

Radhouane, A., N. Mahjoub Said, H. Mhiri, and P. Bournot. 2019. "Wind tunnel experiments of multijets in cross flow: Effect of the injection ratio." *Exp. Therm. Fluid Sci.* 105 (Apr): 234–246. https://doi.org/10.1016/j.expthermflusci.2019.04.007.

Ryan, K. J., J. Bodart, M. Folkersma, C. J. Elkins, and J. K. Eaton. 2017. "Turbulent scalar mixing in a skewed jet in crossflow: Experiments and modeling." *Flow Turbul. Combust.* 98 (3): 781–801. https://doi.org/10.1007/s10494-016-9785-7.

Santiago, J., and J. Dutton. 1997. "Crossflow vortices of a jet injected into a supersonic crossflow." *AIAA J.* 35 (5): 915–917. https://doi.org/10.2514/2.7468.

Sathiyamoorthy, K., T. H. Danish, V. S. Iyengar, J. Srinivas, X. Harikrishna, T. M. Muruganandam, and S. R. Chakravarthy. 2020. "Penetration and combustion studies of tandem liquid jets in supersonic crossflow." *J. Propul. Power* 36 (6): 920–930. https://doi.org/10.2514/1.B38047.

Schetz, J. A., A. K. Jakubowski, and K. Aoyagi. 1983. "Jet trajectories and surface pressures induced on a body of revolution with various dual jet configurations." *J. Aircr.* 20 (11): 975–982. https://doi.org/10.2514/3.48201.

Shaw, V. G., R. Holpp, N. Stocker, J. Coffey, B. Wozniak, E. Gutmark, A. Gaetano, and T. Pritschau. 2020. "Breakup characteristics and far-field trajectory of liquid jets in subsonic crossflow." In *Proc., AIAA Propulsion and Energy 2020 Forum*. Reston, VA: American Institute of Aeronautics and Astronautics.

Towne, A., O. T. Schmidt, and T. Colonius. 2018. "Spectral proper orthogonal decomposition and its relationship to dynamic mode decomposition and resolvent analysis." *J. Fluid Mech.* 847 (Jul): 821–867. https://doi.org/10.1017/jfm.2018.283.

Yu, D., M. S. Ali, and J. H. W. Lee. 2006. "Multiple tandem jets in crossflow." *J. Hydraul. Eng.* 132 (9): 971–982. https://doi.org/10.1061/(ASCE)0733-9429(2006)132:9(971).

Yuan, L. L., and R. L. Street. 1998. "Trajectory and entrainment of a round jet in crossflow." *Phys. Fluids* 10 (9): 2323–2335. https://doi.org/10.1063/1.869751.

Zhao, K., S. Alimohammadi, P. N. Okolo, J. Kennedy, and G. J. Bennett. 2018a. "Aerodynamic noise reduction using dual-jet planar air curtains." *J. Sound Vib.* 432 (Oct): 192–212. https://doi.org/10.1016/j.jsv.2018.06.036.

Zhao, K., Y. Liang, P. N. Okolo, Y. Wang, Z. Wu, and G. J. Bennett. 2020a. "Suppression of aerodynamic noise using dual-jet air curtains combined with perforated fairings." *Appl. Acoust.* 158 (Jan): 107042. https://doi.org/10.1016/j.apacoust.2019.107042.

Zhao, K., P. Okolo, E. Neri, P. Chen, J. Kennedy, and G. J. Bennett. 2020b. "Noise reduction technologies for aircraft landing gear—A bibliographic review." *Prog. Aerosp. Sci.* 112 (Jan): 100589. https://doi.org/10.1016/j.paerosci.2019.100589.

Zhao, K., P. N. Okolo, Y. Wang, J. Kennedy, and G. J. Bennett. 2018b. "An experimental characterization of the interaction between two tandem planar jets in a crossflow." *J. Fluids Eng.* 140 (11): 111106. https://doi.org/10.1115/1.4040224.